Imaging interfacial topography with coherent x-ray reflectivity

Paul Fenter[1,*] and Irene Calvo Almazán[2]
[1]*Chemical Sciences and Engineering Division, Argonne National Laboratory, Lemont, Illinois 60439, USA*
[2]*Institute of Nanosciences and Materials of Aragon (INMA), University of Zaragoza, Zaragoza, Spain*

(Received 1 December 2023; accepted 12 February 2024; published 19 March 2024)

The use of coherent x-ray reflectivity to image interfaces is illustrated using model calculations for three cases: a thin film, a semi-infinite substrate, and a coherently strained epitaxial thin film. The intensities and phases of the coherent scattering signals are calculated based on a fully atomistic model (where the phases are assumed to have been recovered by a phasing algorithm). We describe the characteristics of the effective density that are obtained by direct inverse Fourier transformation of the complex structure factors, using a window function to define the data range. These effective densities include significant artifacts like oscillations and negative values derived from the finite vertical momentum transfer of the window function. Two approaches are described to extract the surface topography from the effective densities for three-dimensional visualization: (i) multiplying the effective density by a phase factor and (ii) analyzing the data as a hybrid structure factor $F(x, Q_z)$. The explicit surface sensitivity and specificity of measurements is illustrated when the film or substrate Bragg peaks are excluded. These considerations show that images of interfacial topography can be obtained using currently available experimental capabilities with parameters corresponding to epitaxial thin films.

DOI: 10.1103/PhysRevB.109.094112

I. INTRODUCTION

The use of x-ray coherence to image materials has led to a revolution in the ability to observe and probe aperiodic structures. After the conceptual definition of oversampling by Sayre [1] and the development of phasing algorithms to recover the unmeasured phase [2], Miao and Sayre [3] and Miao *et al.* [4,5] demonstrated the concept of using diffuse scattering to image nonperiodic structures through phase retrieval from measured intensities. This concept has since been extended to individual crystalline nanoparticles [i.e., Bragg coherent diffraction imaging (BCDI)] [6–8], interfacial coherent scattering [9–11], as well as ptychographic reconstructions of complex (crystalline and noncrystalline) extended structures [12–14]. Significant advances have also been made in probing interfacial dynamics using x-ray photon correlation spectroscopy (XPCS) [15], including observations during epitaxial growth [16–18] and etching [19]. Of these areas, the use of coherent scattering to image interfacial structure and topography is perhaps the least well developed and has been hindered by inherently weak scattering signals coupled with the limited coherent flux from third-generation x-ray sources. The advent of fourth-generation x-ray synchrotron facilities such as MAX-IV [20], the ESRF-EBS [21], the APS-U [22], and other facilities is leading to increases of 2–3 orders of magnitude in the coherent flux at hard x-ray energies [23]. In this context, the use of coherent x-rays to probe interfaces will become increasingly powerful especially since interfacial signals are weak and require a high flux to be observed. Substantial improvements can be expected in the ability to probe interfacial dynamics with XPCS and more specifically in its enhanced time resolution which can potentially reach the microsecond time scale thanks to the signal-to-noise ratio rising quadratically with the gain in coherent flux [24,25]. These advances in coherent sources will also strongly impact the ability to image the extended structure and topography of interfaces using variations of BCDI and ptychographic imaging [23].

In their seminal work, Vartanyants *et al.* [9] demonstrated the concept of imaging surface topography by laterally oversampling the reflectivity signal in the low-angle (i.e., Fresnel) regime. Such measurements, which were performed at grazing incidence, are challenged by the extended incident beam footprint that is intrinsic to the small grazing angle of incidence. Zhu *et al.* [10] and Pierce *et al.* [11] extended this concept to the crystal truncation rod (CTR) regime. While successful in observing the location of steps, the height of each terrace was not recovered. Also, the recovered amplitudes exhibited nonuniform interfacial values from a nominally uniform substrate. This likely derives from an important simplifying assumption, in which they phased detector images obtained in the reflection geometry using algorithms that were developed to phase forward scattering data (i.e., near $Q = 0$). However, there is an important difference between data obtained in the forward scattering and reflection geometries. Scattering intensities exhibit inversion symmetry, i.e., $I(\mathbf{Q}) = I(-\mathbf{Q})$, as defined by Friedel's law [26], where $\mathbf{Q}$ is the momentum transfer vector. In the forward scattering geometry, this is apparent within any detector image since the range of momentum transfer probed is centered on the origin of reciprocal space. In contrast, detector images in a reflectivity measurement are inherently asymmetric because the momentum transfer within the detector plane (i.e., Ewald sphere) is

*fenter@anl.gov

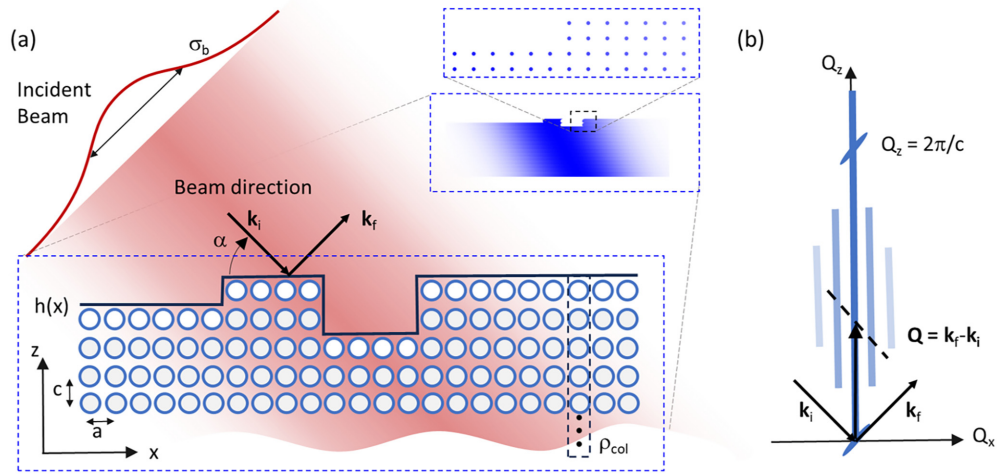

FIG. 1. Scheme of a coherent reflectivity measurement: (a) A coherent incident beam (with a transverse size σ_b) is incident (at an angle α) on an interface, defined by a height function $h(x)$, with vertical and lateral lattice spacings of c and a. The shape of the illuminated density is defined by a combination of the top and bottom interfaces of the film as well as the lateral illumination defined by the beam (insets for the full object and a detail of a single step). (b) Schematic of the reciprocal space structure (as a function of lateral and vertical momentum transfers Q_x and Q_z) including Bragg peaks (at $Q_z = 0$ and $2\pi/c$), specular truncation rod (with a lateral width controlled by the beam illumination within the surface plane $\sigma_b/\sin(\theta)$, where σ_b is the transverse width of the beam) and elongated speckles parallel to the crystal truncation rod (CTR). The scattering geometry is shown (with incident k_i and reflected k_f beams), and the Ewald sphere (dashed line) indicates the range of momentum transfers probed at a fixed scattering geometry.

centered on a point along the CTR and is tilted away from the surface normal direction by the incident angle defined by the specular reflection condition. Consequently, any asymmetry in the measured detector image will be explained by the forward phase retrieval algorithm by the inclusion of a complex interfacial density for internal consistency but which will be an artifact.

An important feature of interfacial scattering is that topography is a pure phase object of the form $\exp[iQ_z h(x)c]$ [9,27–29], where Q_z is the vertical momentum transfer, $h(x)$ is the surface height function, an integer valued function of position x, and c is the vertical lattice spacing (Fig. 1). Consequently, it can be expected that topography will be encoded in the phase of the interfacial scattering intensities. This has been demonstrated in the use of x-ray reflection interface microscopy (XRIM) in which the reflected surface topography was imaged with an incoherent x-ray beam focused through an objective lens [28]. This result shows that information about the topography (i.e., the location of each step and the height of each terraces) is encoded in the localized variation of the spatially resolved reflected intensity across each step in the recovered image and derives from the interference between x rays reflected from these neighboring terraces [29].

Here, model calculations are presented to identify the information content that can be obtained from coherent reflectivity measurements once the complex phases of the scattered intensities have been recovered through the use of phase recovery algorithms [30,31]. We consider the idealized case in which the intensities are measured within an extended reciprocal space region of a one-dimensional (1D) crystalline surface that is periodic within the surface plane (except for topographic variations in the surface height) and that is either finite or semi-infinite along the surface normal direction (corresponding to thin films, surfaces, and interfaces). The extension to three-dimensional (3D) imaging of two-dimensional (2D) interfaces is obvious. The focus of the discussion includes (i) describing the characteristics of the effective densities obtained from the inverse Fourier transform (FT) of complex structure factors and (ii) extracting intrinsic characteristics of the interfacial and thin-film topography from these effective densities. We also illustrate the mechanism of interfacial specificity that derives from the effective density. We assume, for simplicity and without loss of generality, that the termination of the substrate is the same at every surface site, i.e., the substrate density can be described by the same column of density $\rho_{\rm col}$, except for a vertical displacement by an integer multiple of the layer spacing c, to describe the surface topography $h(x)$ (Fig. 1). For computational convenience, we also assume that the lattice termination is bulklike, i.e., every atom is in a bulk unit-cell position, although incorporation of realistic features such as surface relaxations and reconstructions is straightforward.

II. COHERENT CTR SCATTERING FROM SURFACES AND THIN FILMS USING KINEMATIC SCATTERING

Consider the case of a fully coherent x-ray beam (with energy E) incident at an interface with a fixed angle α, on an interfacial density $\rho(x,z) = \Sigma_j \rho_j(x,z)$, where ρ_j is the atomic density of atom j located at $[x,z] = [x_j, z_j]$ [as shown schematically in Fig. 1(a)]. For simplicity, these calculations are limited to a 1D interface within the $x-z$ plane that corresponds to the scattering plane, where x is the in-plane coordinates, while z is perpendicular to the surface plane. The incident beam wave vector is $\mathbf{k}_i = k\mathbf{u}_i$ (where $|\mathbf{k}_i| = k = E/\hbar c$ and $\hbar c = 1973\,\text{ev Å}$) and $\mathbf{u}_i$ is the unit

vector corresponding to the incident beam direction defined by α. These calculations assume a coherent beam illumination magnitude having a Gaussian transverse shape $A(x, x_0, z) = G\{[(x - x_0) - z/\tan(\alpha)]/\sigma_b\}$, which characterizes the beam intensity above and below the surface for a transverse beam width σ_b. The shape of the beam within the surface plane, at $z = 0$, $A(x, x_0, 0)$, defines the surface illumination function whose maximum corresponds to the beam position x_0 in the surface plane and has a lateral size $\sigma_{bx} = \sigma_b/\sin(\alpha)$. Here, we consider the idealized case in which the beam is real valued. The inclusion of a complex-valued beam profile (i.e., due to beam focusing) can be performed without any loss of generality.

The film or surface has a lattice structure that is defined by the lateral and vertical lattice spacings (a and c, respectively) with a surface topography $h(x)$ and either a semi-infinite substrate or a finite film with a flat bottom surface (more generally, the bottom surface has its own surface height function). These calculations assume a transverse beam width $\sigma_b = 20a$ (where $a = 3$ Å), although the specific value of the width is unimportant whenever the reciprocal space data are oversampled to allow for the phasing of the intensities. The product of the film density and the illumination field defines the illuminated object that is being imaged [Fig. 1(a), inset]. Within this model, the object is bounded vertically by the actual top and bottom interfaces of the film and laterally by the finite width of the illumination function.

The scattering condition is defined by the vector momentum transfer $\mathbf{Q} = \mathbf{k}_f - \mathbf{k}_i = [Q_x, Q_z]$ (Fig. 1). Within kinematic scattering theory, the scattering signals are calculated by the structure factor $F(Q_x, Q_z)$:

$$\begin{aligned} F(Q_x, Q_z) &\equiv \int_{x,z} A(x, x_0, z)\rho(x, z)\exp[i(Q_x x + Q_z z)]dz\, dx, \\ &= \sum_j A(x_j, x_0, z_j)\ \rho(x_j, z_j)\exp[i(Q_x\, x_j + Q_z\, z_j)] \\ &= \sum_j f_j(Q)\, A(x_j, x_0, z_j)\exp[i(Q_x\, x_j + Q_z\, z_j)]. \end{aligned} \tag{1}$$

Here, $f_j(Q)$ is the atomic scattering factor for atom j. The scattering intensity can then be calculated as

$$I(Q_x, Q_z) = |F(Q_x, Q_z)|^2. \tag{2}$$

The calculated intensities have features that are expected for interfacial and thin-film scattering [as shown schematically in Fig. 1(b)], including the Bragg peaks at $Q_x = 0$ and $Q_z = 2\pi/c$, a surface truncation rod (CTR) located at $Q_x = 0$, and nonspecular (i.e., diffuse) scattering deriving from the surface roughness (for $|Q_x| > 0$). While the diffuse scattering intensities would be largely featureless when probed by an incoherent beam, they appear as speckles when probed with a coherent beam. These speckles are laterally sharp (having a width $\Delta Q_x \sim 2\pi/\sigma_{bx}$, controlled by the lateral beam footprint σ_{bx}) but elongated along the surface normal direction [32]. Note that the use of Eq. (1) assumes that the scattering intensities and structure factors are defined solely by the momentum transfer $\mathbf{Q}$ and implicitly assumes that the incident beam direction (e.g., angle of incidence) is fixed. Instead, measurements typically sample reciprocal space by systematically varying the incident angle.

III. IMAGING THIN FILM AND INTERFACIAL STRUCTURES

A. Imaged structure as an effective density

Images of an interface probed by coherent x-ray scattering are obtained in two steps: first by phasing the experimental scattering intensities that define the magnitude of the complex structure factor. Second, the unknown structure is imaged by inverse FT, the complexed valued structure factor:

$$\begin{aligned} \rho_{\text{eff}}(x, z) &= \int_{Q_x,Q_z} W(Q_x, Q_z)F(Q_x, Q_z) \\ &\quad \times \exp[-i(Q_x x + Q_z z)]dQ_x\, dQ_z \\ &= W(x, z) \otimes \rho(x, z). \end{aligned} \tag{3a}$$

$$W(x, z) = \textstyle\int_{Qx}\int_{Qz} W(Q_x, Q_z)\exp[-i(Q_x x + Q_z z)]dQ_z\, dQ_x \tag{3b}$$

Here, we define $F(Q_x, Q_z) = [I(Q_x, Q_z)]^{1/2}\ \exp[i\Phi(Q_x, Q_z)]$, where $[I(Q_x, Q_z)]^{1/2}$ is the structure factor amplitude and $\Phi(Q_x, Q_z)$ is the associated phase (i.e., recovered by a phasing algorithm). In this expression, the integration range includes all reciprocal space. However, the measurement range is indicated by a window function $W(Q_x, Q_z)$. Since the choice of $W(Q_x, Q_z)$ has a direct impact on the details of the recovered object, we refer to the recovered density as an effective density, a reminder that it is necessary to explicitly account for those details in interpreting the resulting image and to extract the characteristics of the original object from the effective density. This is emphasized in the second part of Eq. (3), where the effective density can also be written as the convolution of the intrinsic density $\rho(x, z)$ and the real-space window function, $W(x, z)$, which is the FT of the reciprocal space window function $W(Q_x, Q_z)$. From this perspective, it is apparent that the finite range of the measurement can have a direct bearing on the details of the effective density.

B. Imaging thin films

We begin with the case of scattering from an unsupported film, as the structure factor can be calculated directly from Eq. (1). Three thin-film structures are considered [Figs. 2(a)(i)–2(a)(iii)] to illustrate the key features of coherent interfacial x-ray imaging. These include (i) a flat thin-film structure with $N_{\text{film}} = 15$ layers, illuminated by an x-ray beam at an incident angle of 45°; (ii) a rough film with a variable surface height [defined by the height function $h(x)$]; and (iii) the same rough film illuminated by a beam at an incident angle of 90° which maintains the same lateral footprint and whose magnitude produces the same flux. Consequently, the results in Figs. 2(a)(iii) are directly comparable with those in Figs. 2(a)(i) and 2(a)(ii). The illuminated volumes (i.e., the product of the density with the illumination) are shown in Fig. 2(a), and the corresponding intensities calculated numerically using Eq. (3) are shown in Fig. 2(b). For the uniform thin film [Fig. 2(b)(i)], the intensities show the expected behavior with a laterally narrow CTR that connects the thin-film Bragg

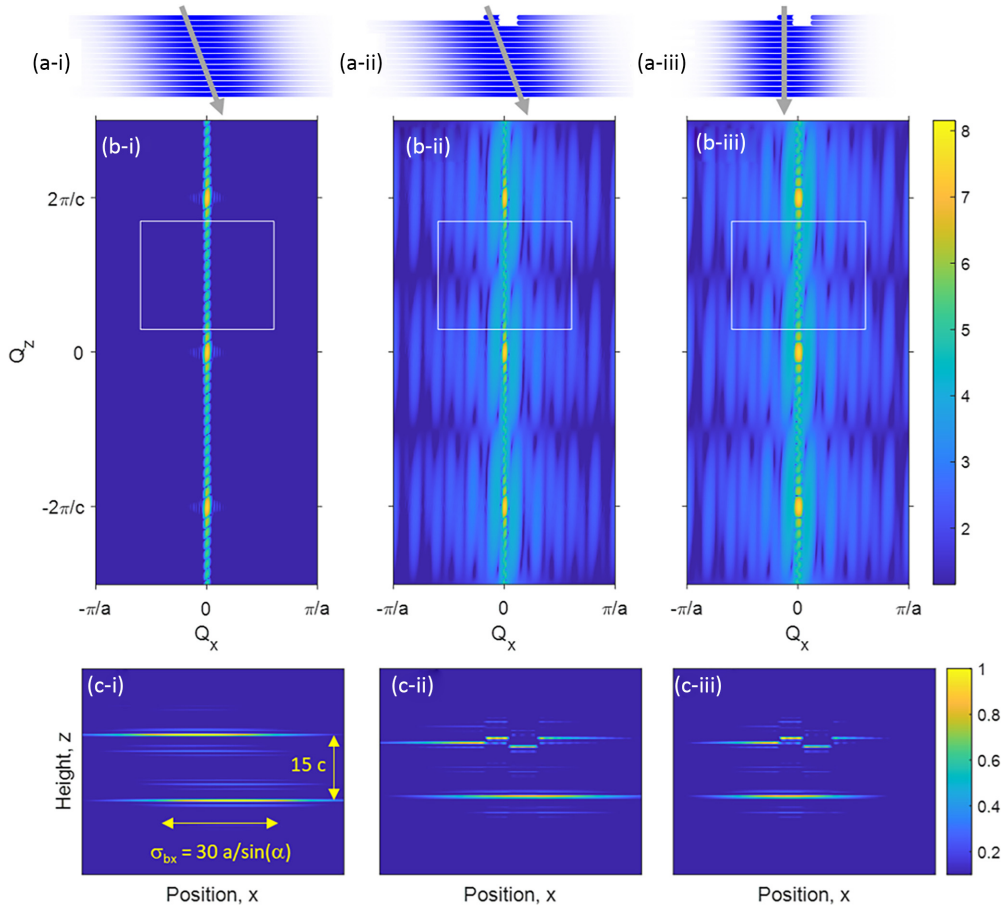

FIG. 2. Illuminated structures, reciprocal space structure, and effective densities: (a) Illuminated thin-film structures for (i) a flat thin film and (ii) a rough film (both with an incident beam illumination at $\alpha = 45^\circ$), and (iii) the same rough film with vertical illumination ($\alpha = 90^\circ$). The uniform film is 15 unit cells thick, and the roughness corresponds to changes in the surface height of $-1c$ and $-2c$, as shown. (b) Reciprocal space structures presented as calculated scattering intensities (shown as $\log_{10}[I(Q_x, Q_z)]$), calculated using Eqs. (1) and (2). The white box is the region of interest (ROI) used to sample the scattered intensities ($Q_{0z} = 0.5Q_B$, $\delta Q_z = 0.7Q_B$, where $Q_B = 2\pi/c$ is the momentum transfer at the Bragg peak position). (c) The recovered images corresponding to the real part of the effective densities for each of the illuminated structures shown in (a) with a threshold of 10% of the maximum density.

peaks at $Q_z = \pm 2\pi/c$ and whose lateral size is controlled by the in-plane width of the illumination function σ_{bx}. The CTR also shows intensity oscillations along the specular rod with a period $\Delta Q_z = 2\pi/N_{\text{film}}c$ corresponding to the thin film having a thickness of $N_{\text{film}} = 15$. In addition, these oscillations are skewed (i.e., the locations of the minima in Q_z depend on the value of Q_x) as a direct result of the tilted incident beam illumination $A(x, x_0, z)$.

As expected from the discussion concerning Eqs. (1) and (2), the scattering intensities for the film with a rough surface [Fig. 2(b)(ii)] also include diffuse scattering in the form of speckles that are laterally sharp (but broader than the CTR due to the smaller average size of the illuminated surface domains with respect to the beam footprint) and elongated along the surface normal direction. The role of the incident beam direction is illustrated by comparing these results to the intensities obtained from the same rough film with an incidence beam at normal incidence [Fig. 2(b)(iii)], where the calculated scattering intensities are nearly identical to those for the tilted beam [Fig. 2(b)(ii)] except for differences near the thin-film Bragg peaks and the surface truncation rod. Most notably, the Kiessig fringes along the specular rod are tilted to be orthogonal to the incident beam direction. In comparison, the diffuse scattering signals at momentum transfer values away from the specular truncation rod appear to be unaffected by the choice of the beam direction. This illustrates that these interfacial coherent scattering signals along the CTR are sensitive not only to momentum transfer **Q** but also to the specific beam direction α and that care needs to be considered properly for these details.

The effective densities [Fig. 2(c)] are obtained by inverse FT of the complex structure factor using a window function that includes a broad segment of the CTR along Q_z [white boxes in Fig. 2(b)]. For this example, the region of interest (ROI) is centered vertically at $Q_{0z} = \frac{1}{2}Q_B$ (where $Q_B = 2\pi/c$) with a vertical window size $\delta Q_z = 0.7Q_B$ and laterally at $Q_{0x} = 0$ with a lateral window size $\delta Q_x = 1.2\pi/a$. Inclusion of the mirrored window, centered at $Q = -Q_{0z}$ (not shown), ensures that the effective density is a real-valued function. These images show the positive real-valued part of the effective densities with a threshold corresponding to 10% of the maximum effective density. The effective density of the flat film [Fig. 2(c)(i)] shows the two flat and counterpoised surfaces of the film that are sharp but also include multiple

fringes along the surface normal direction z. As expected, the top and bottom surfaces are laterally displaced, corresponding to the regions of the film that are illuminated by the incident beam. This image can be compared with the effective density obtained for the rough film [Fig. 2(c)(ii)], which is essentially the same in all respects except that the height of the top surface varies with position, directly following the topography of the original surface object (while the bottom surface remains unaffected). This confirms that the reflectivity data, properly phased, images the topography of an isolated film, albeit with artifacts corresponding to negative densities and layers of effective density that are parallel to the surface (these are discussed in more detail below). Finally, the image obtained from the nontilted beam with the rough surface [Fig. 2(c)(iii)] is essentially identical to that obtained with the tilted beam, except that the lateral location of the bottom surface is shifted laterally corresponding to the intersection of the beam with the bottom surface. These differences are controlled by the small differences in the skewness of the oscillations on the specular rod, most notably near the film Bragg peak, as identified above. In other words, these images immediately reveal that the coherent CTR signals are not only interface sensitive, but they are also interface specific (i.e., they derive only from the interface).

It is useful to consider the resolution of the data in interpreting these images. A simple estimation of resolution can be obtained from the range of reciprocal space that is probed (i.e., the same consideration that defines a microscope resolution from its numerical aperture [33]), which can be written $\delta r \approx 2\pi/\delta Q$. These images therefore have a vertical resolution of $\sim 1.1c$, while the lateral resolution is $\sim 1.7a$. The lateral atomic layer spacing within the crystal is therefore not resolved, and the interfaces are seen as a continuous density within the surface plane. In contrast, the vertical resolution nearly resolves the individual atomic layers, but the images display what appears to be a single layer that defines the surface plane. The generality of this observation is explained below (Sec. III F).

C. Imaging the interface of a semi-infinite crystal

Extending these observations to a semi-infinite crystal requires a closed-form expression for the structure factor of a coherent CTR. The distinguishing character of a coherent CTR is the explicit inclusion of the spatial extent of the incident beam rather than the laterally infinite plane-wave beam that is normally assumed. A closed-form expression for the case of a flat semi-infinite crystal can be derived in the limit of a simple lattice having a flat and bulklike termination in which all atoms in a given column are identical and separated by the bulk layer spacing c (the extension to the case where the substrate unit cell has multiple atoms can be accounted for by inclusion of a unit cell form factor). The difference in the illuminated structure between subsequent layers involves a vertical shift of the layer (corresponding to a single layer spacing c) and a lateral shift of the illumination function, by $c/\tan(\alpha)$, where α is the angle of incidence [the illuminated structure is shown in Fig. 3(a)]. From these considerations, the coherent CTR form factor for the specular truncation rod can

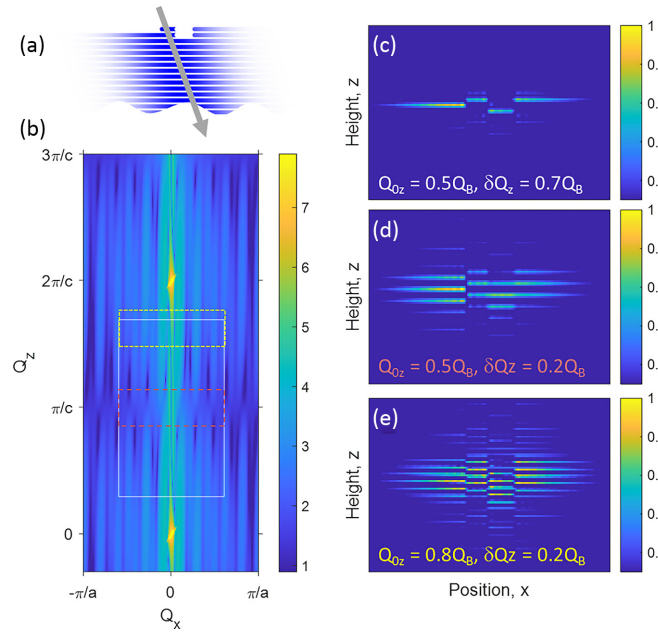

FIG. 3. Role of the region of interest (ROI) on the imaged effective density: (a) Illuminated semi-infinite interface (with the same surface roughness from Fig. 2 and $\alpha = 45°$) and (b) the associated reciprocal space structure (displayed as $\log_{10}[I(Q_x, Q_z)]$ and calculated using Eqs. (1) and (2). Three ROIs are indicated (white box: $Q_{0z} = 0.5Q_B$, $\delta Q_z = 0.7Q_B$; red-dashed box: $Q_{0z} = 0.5Q_B$, $\delta Q_z = 0.2$; yellow-dashed box: $Q_{0z} = 0.8Q_B$, $\delta Q_z = 0.2Q_B$, where $Q_B = 2\pi/c$ is the momentum transfer at the substrate Bragg peak position). The real part of the effective densities for the three ROIs are shown in (c)–(e) with a threshold corresponding to 10% of the maximum density.

be derived:

$$F_{c\mathrm{CTR}}(Q_x, Q_z) = \frac{A_0 \exp\{-(Q_x\,\sigma_{bx})^2\}\exp(iQ_x x_0)}{1 - \exp\{-i[Q_z - Q_x/\tan(\alpha)]c\}}, \tag{4}$$

where A_0 is a scale factor. Comparing this expression with that for incoherent reflectivity, i.e., the well-known CTR form factor, $F_{\mathrm{CTR}} = 1/[1-\exp(-iQ_z c)]$ reveals that the coherent CTR has a Debye-Waller term, $\exp[-(Q_x\,\sigma_{bx})^2/2]$, that derives from the lateral extent of the beam σ_{bx} an overall phase $\exp(iQ_x x_0)$ that is controlled by the beam position x_0. The denominator of the CTR term contains the term $Q_z - Q_x/\tan(\alpha)$ rather than Q_z which accounts for the tilt of the beam.

Within the assumption of an ideal bulklike terminated surface, the structure factor of a rough surface can be obtained by making use of the additivity properties of the structure factor:

$$F_{\mathrm{rough}} = F_{c\mathrm{CTR}} + \Delta F_{\mathrm{rough}}, \tag{5a}$$

$$\Delta F_{\mathrm{rough}}(Q_x, Q_z) = \sum_j f_j(Q) A(x_j, x_0, z_j)\Delta O_j \times \exp\{i(Q_x x_j + Q_z z_j)\}. \tag{5b}$$

Here, $\Delta F_{\mathrm{rough}}(Q_x, Q_z)$ is a differential structure factor that adds or removes atoms from the surface to create a rough surface. Consequently, ΔO_j is the change in occupation factor of each atom j, with respect to the flat surface (i.e., $\Delta O_j = 1$ or

−1 corresponds to atoms that are added on top of, or removed from within, a flat surface, respectively). Through this approach, we can calculate the scattering intensities [Fig. 3(b)] using the same surface topography considered above (Fig. 2). The similarity in the diffuse scattering intensities of the rough semi-infinite surface (Fig. 3) and the rough film (Fig. 2) is immediately obvious and expected since the bottom surface of the film did not contribute to those signals, but there are notable differences from the thin films. These include a CTR that consists of continuous vertical streaks (rather than the modulated intensity along Q_z). Also, the CTR is laterally split near the anti-Bragg condition (i.e., at $Q_z = \pi/c$) due to tilted rods of intensity that originate from the Bragg peaks (at $Q_z = 0$ and $Q_z = Q_B$, where $Q_B \equiv 2\pi/c$) associated with the local miscut of the illuminated surface. Finally, the sharp substrate Braggs peaks are asymmetrically broadened with tilted diffuse streaks in the direction transverse to the beam direction. The effective density [Fig. 3(c)] is recovered using a window function [white box, Fig. 3(b)] that is the same as that used for the case of the thin film [Fig. 2(c)]. This image shows an effective density that appears identical to that obtained for the case of the thin film except for the absence of the bottom interface.

This calculation scheme enables us to evaluate the role of the window function on the effective densities for a rough semi-infinite surface. The effective density (with a threshold of 10% of the maximum density) obtained from the large window located at the anti-Bragg position [Fig. 3(c), $Q_{0z} = Q_B/2$ and $\delta Q_z = 0.7Q_B$] is compared with a smaller window function centered (i) at the anti-Bragg condition [Fig. 3(d), at $Q_{0z} = Q_B/2$, with $\delta Q_z = 0.2Q_B$, and a corresponding resolution of $\delta r = 5c$] and (ii) at an arbitrary location [Fig. 3(e), $Q_{0z} = 0.8Q_B$, with $\delta Q_z = 0.2Q_B$]. In all cases, the interfacial topography can be clearly seen as a vertical shift of the effective density, although the details of the effective density are distinct for the three choice of window locations. The choice of a smaller vertical window size leads to an image with more broadly distributed fringes along Q_z [Figs. 3(d) and 3(e)] consistent with its lower spatial resolution, suggesting that interface is no longer well resolved in the vertical direction. Note also that the spacing of the fringes along z depends directly on the window location Q_{0z}.

D. Extracting the surface height from the effective density

The results in the previous section reveal that interface images obtained from coherent reflectivity data are strongly influenced by the details of the experimental measurement [i.e., the shape and location of the window function $W(Q_x, Q_z)$]. While such images may be useful in themselves (since the topography can be inferred visually), it is valuable to extract quantitative information from these effective densities. In this respect, there are two challenges to be addressed. First, the extended shape of the CTRs along the surface normal (Q_z) direction implies that the window function can lead to truncation artifacts in the effective density. Furthermore, we can expect that the vertical window size will typically be smaller than the spacing between Bragg peaks, and therefore, the atomistic structural features of the interface are unlikely to be resolved. In this section, we consider approaches to extract the surface height function $h(x)$ and the effective illumination function $A_{\rm eff}(x)$ from these effective densities.

We begin by considering the real-space window function $W(z)$ along the surface normal direction. This can be calculated in general for a window location Q_{0z} and a window range δQ_z as

$$W(z) = \exp(-iQ_{0z}z)\delta Q_z\left[\frac{\sin(\delta Q_z z/2)}{\delta Q_z z/2}\right] = \exp(-iQ_{0z}z)W_0(z). \tag{6a}$$

$$W_0(z) = \delta Q_z\left[\frac{\sin(\delta Q_z z/2)}{\delta Q_z z/2}\right] \tag{6b}$$

This function is complex because we considered only the window at $+|Q_{0z}|$. Here, $W_0(z)$ is the equivalent expression of the same window function centered at $Q_{0z} = 0$. It controls the broadening of the effective density as defined by the data range δQ_z. This is inherent to any imaging measurement and is seen as an envelope function that broadens the effective density. Equation (6) also shows that measurements centered at nonzero Q_{0z} lead to an additional phase factor $\exp(-iQ_{0z}z)$. Since the effective density is the convolution of the density with the window function [e.g., as shown in Eq. (3)], this term leads to high-frequency modulations of the effective density. Note that the periodicity of these oscillations is defined by the choice of Q_{0z} [as seen by comparing Figs. 3(d) and 3(e)]. For example, the periodicity of the real-space window function at $Q_{0z} = \pi/c$ is exactly twice the layer spacing $2c$, as expected from Eq. (6).

A strategy for dealing with these features can be adapted from BCDI imaging [34]. There, measurements centered on a Bragg peak (i.e., at $Q_0 = 2\pi/c = Q_B$) have sensitivity to the layer density along the direction of the momentum transfer vector. A continuous effective density is obtained with a change of variables by using a reduced momentum transfer $q = Q - Q_0$ as

$$\rho_{\rm eff}(z) = {\rm FT}^{-1}[F(Q)W(Q)] = \exp[-iQ_0 z]\rho_{{\rm eff}-0}(z). \tag{7}$$

Here, $\rho_{{\rm eff}-0}(z) \equiv \int F(Q_0+q)\,W(Q_0+q)\exp[-iqz]\,dq$ is the effective density that would be obtained by direct FT of the data as if they were centered at the origin [i.e., $Q_0 = 0$; i.e., by using a fast FT (FFT) of the data centered on the Bragg peak]. That term then will be controlled primarily by the effect of resolution broadening. Consequently, a continuous density profile can be obtained from the effective density by

$$\rho_{{\rm eff}-0}(z) = \exp[iQ_0 z]\rho_{\rm eff}(z). \tag{8}$$

Equation (8) reveals that an image of the effective density without the contribution of the high-frequency oscillations, deriving from data at finite Q_{0z}, can be obtained by multiplying the effective density by a phase factor $\exp[iQ_0 x]$. This is confirmed in Fig. 4, where the magnitude of (a) $\rho_{\rm eff}(z)$ and (b) $\exp[iQ_0 z]\rho_{\rm eff}(z)$ are compared (for the case of $Q_{0z} = \pi/c$, $\delta Q_z = 2\pi/5c$ and $\delta Q_x = 1.2\pi/a$). The same topography can be seen both without and with the phase correction, but the image with the phase correction is a continuous function of height z, and therefore, the location of the interface (i.e., the height of the maximum value of the effective density) can more easily be determined. A plot of these two effective

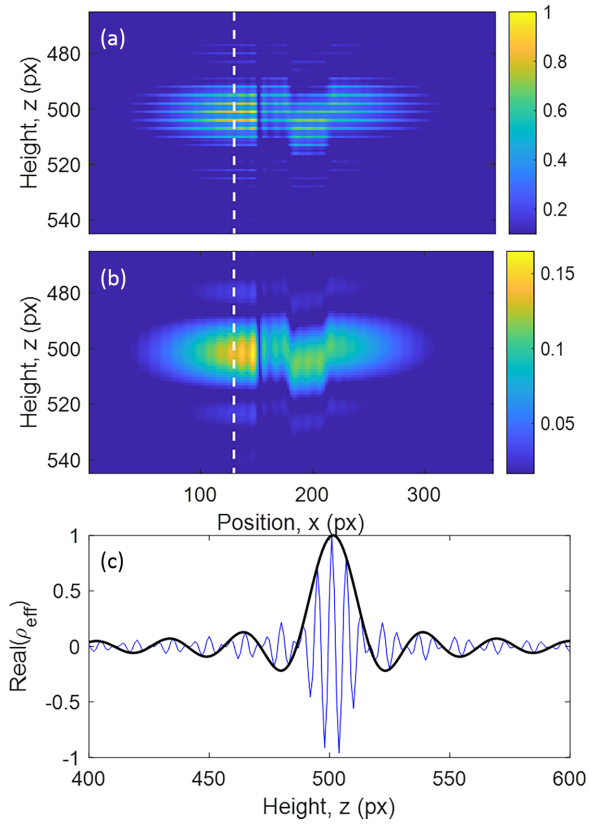

FIG. 4. Removing artifacts: Magnitude of the effective density [obtained using the red region of interest (ROI) in Fig. 3, for a reciprocal space window with $Q_{0z} = 0.5Q_B$, $\delta Q_z = 0.2Q_B$] both (a) without and (b) with the use of a phase shift to remove the high-frequency artifacts (shown with a threshold corresponding to 10% of the maximum density). (c) A comparison of the real part of the effective density (at the lateral location at $x = 125$ px) before and after the phase shift, showing both positive and negative values of the effective density as well as the extended oscillations away from the interface location (located at a height $z \sim 500$ px).

densities as a function of height [Fig. 4(c)] confirms that the phase-corrected density is the envelope function that defines the extrema of the original uncorrected effective density having high-frequency oscillations.

With these details in mind, we can now extract useful information from the effective densities. Figure 5 shows the magnitude of the phase-corrected effective densities obtained by applying Eq. (8) to the effective densities shown in Fig. 3. In all cases, the effective density now reveals the topography without the fine-structure modulations associated with the window function location Q_{0z}. The surface height profile of the effective densities is visually clear and can be extracted by evaluating the height at which this function is maximized at each surface position x or by calculating an average height by numerical integration of the effective density along the z direction $< h(x) >= \Sigma_z z\rho_{\text{eff-0}}(x,z)/\Sigma_z \rho_{\text{eff-0}}(x,z)$, as shown in Figs. 5(a)(iii), 5(b)(iii), and 5(c)(iii). The two approaches give generally similar height profiles albeit with some differences that are due to the finite pixel size of the image of the effective density. The height obtained from the maximum value of the effective density is expected to be less accurate.

The variation of the effective density magnitude is obtained by vertically integrating the effective density [Figs. 5(a)(i), 5(b)(i), and 5(c)(i)] along the surface normal direction $A_{\text{eff}}(x) = \Sigma_z \rho_{\text{eff-0}}(x,z)$ [Figs. 5(a)(ii), 5(b)(ii), and 5(c)(ii)]. This quantity has two contributions. As might be expected, the lateral shape reflects the illumination of the interface (determined by the Gaussian shape of the incident beam and its projected footprint). Superimposed on this Gaussian beam profile are additional modulations that are associated with the location of individual steps [dashed vertical lines, Figs. 5(a)(ii), 5(b)(ii), and 5(c)(ii)]. While these modulations are generally mild perturbations of the illumination function in Figs. 5(a)(ii) and 5(c)(ii), the recovered amplitude in Fig. 5(b)(ii) shows a nearly complete node near $x = 150$ but without any visible modulations near $x = 170$ and 220. This is because the single and double step heights are exactly out of phase and in phase at that specific scattering condition $Q_{oz} = \pi/c$. The sensitivity of these features to the details of the step height and scattering condition is the same as that in imaging interfacial topography using incoherent x-ray beams (e.g., XRIM [28]). Since the structure factor amplitude should be independent of position (except for the illumination function) for a homogenous surface with topography, information about topography from XRIM derives solely from these interfacial modulations that are controlled by the local phase difference between neighboring terraces, as described previously [29].

E. Imaging epitaxial thin films

These ideas can now be extended to the case of an epitaxial thin film. Here, the film structure is assumed to be conformal and in lateral registry with the semi-infinite substrate but with a larger vertical lattice spacing corresponding to the case of a coherently strained film ($a_{\text{film}} = a, c_{\text{film}} = 1.1c$). This strained film has a thickness of 10 atomic layers with a scattering factor that is 50% larger than the substrate $f_{0\_\text{film}} = 1.5f_0$ (Fig. 6). The calculated scattering intensities for this structure are now substantially more complex than observed for the case of either an isolated thin film (Fig. 2) or a bare surface (Fig. 3) with the same topography. The intensities include both the vertical oscillations corresponding to the film thickness but also substantial lateral streaks emanating from the film Bragg peak and associated Kiessig fringes because of the disruption of the internal film structure due to the substrate topography.

The effective densities from this film are obtained for two ROIs of the same size ($\delta Q_z = 0.5Q_B$), one centered at the substrate anti-Bragg condition [$Q_{0z} = 0.5Q_B$, white box, Fig. 6(b)] and the other at $Q_{0z} = 0.7Q_B$ [yellow dashed box, Fig. 6(b)] so that the ROI includes the thin-film Bragg peak. The effective density for $Q_{0z} = 0.5Q_B$, both without [Fig. 6(c)(i)] and with the phase shift [Fig. 6(c)(ii)], reveals the top surface and film-substrate interface, very similar to that obtained for an isolated thin film. One important difference is that the observed magnitude of the effective density at the film-substrate interface is reduced by the destructive interference between the film and substrate lattices. This can be understood qualitatively by noting that no distinct interface would be observed in the effective density in the limit where the film has the same scattering factor and lattice spacing

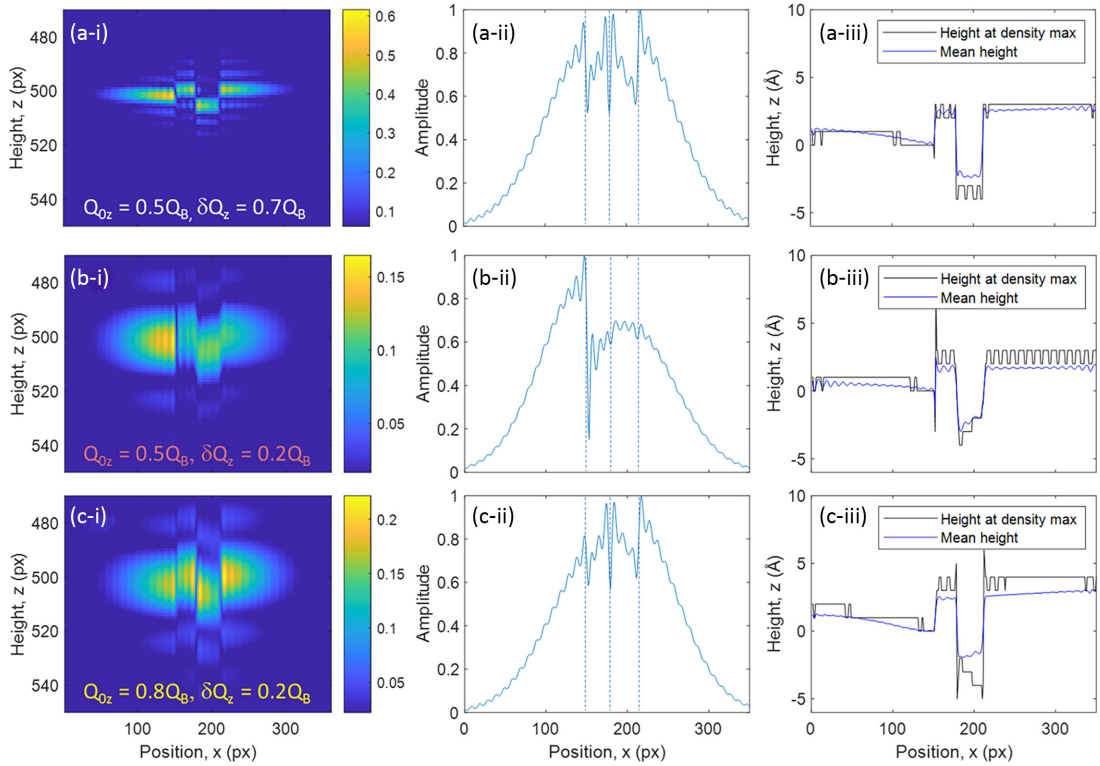

FIG. 5. Recovering the surface topography and effective illumination amplitude: Column (i) magnitude of the effective densities (with a threshold set to 10% of the maximum density); column (ii) recovered amplitudes; and column (iii) height profiles obtained for the three regions of interest (ROIs) in Fig. 3: (a) $Q_{0z} = 0.5Q_B$, $\delta Q_z = 0.7Q_B$; (b) $Q_{0z} = 0.5Q_B$, $\delta Q_z = 0.2Q_B$; (c) $Q_{0z} = 0.8Q_B$, $\delta Q_z = 0.2Q_B$, where $Q_B = 2\pi/c$ is the momentum transfer at the substrate Bragg peak position. The dashed vertical lines in the recovered amplitudes correspond to the step locations.

as the substrate, a situation in which the two contributions would exactly cancel. It is apparent from these images that we can separately quantify the topography of the top and bottom film surfaces using the approach described above (Fig. 5). Therefore, we can expect that interfaces having a variable film thickness (i.e., a nonconformal film) would be immediately apparent by direct inspection of the phase-shifted effective densities. In comparison, the effective density obtained with an ROI at $Q_{0z} = 0.7Q_B$ (i.e., which includes the thin-film Bragg peak) now images the full extent of the thin-film structure [Fig. 6(d)(i)], and the beam illumination is clearly seen in the lateral variation of the effective density magnitude after phase shift [Fig. 6(d)(ii)].

F. Mechanism for interfacial sensitivity

Since any density distribution can be written as a superposition of the contributions from individual atoms, the effective density can also be viewed as the summation of the (complex valued) effective densities from each atom. This is a useful approach to understand how the reflectivity data for a defect-free substrate or thin film only sees the interfaces (as indicated by the effective densities) even though all atoms below the top surface are illuminated by the incident beam. Consider the specific example of imaging a single atom (i.e., along the z direction). In the case where the measurement range does not resolve the intrinsic shape of the atom, the atomic density can be approximated as a delta function $\rho(z) = \delta(z - z_0)$. In this case, we can derive the effective density:

$$\rho_{\text{eff}}(x, z) = W(z) \otimes \delta(z - z_0) = \exp[-iQ_{0z}z] \exp[-iQ_{0z}z_0] W_0(z - z_0). \quad (9)$$

Comparison with Eq. (7) shows that the effective density includes the usual interference function to account for broadening W_0, centered at $z = z_0$, multiplied by a phase term $\exp[-iQ_{0z}z]$ (and a fixed complex phase $\exp[iQ_{0z}z_0]$). When $Q_{0z} = 2\pi/c$, the phase term modulates the density along z with a period of c. Thus, for two atoms (or equivalently layers) separated in z by a separation c, the two layers add constructively since their phases at each position z are identical, with a total density that is nearly double that of an individual layer [Fig. 7(a)]. The summation of 15 atomic layers (as in the example in Fig. 1) leads to a slab of density where the individual atomic contributions are not observed but in which the effective density includes oscillations that are observed both within the slab and outside [Fig. 7(b)]. In contrast, the same analysis for $Q_0 = \pi/c$ (i.e., the midzone position) shows that the effective density of neighboring atoms has a relative phase shift of π at every point, leading to destructive interference. The sum of the effective densities of the two neighboring atoms therefore has a node at the midpoint between the two atoms [black line, Fig. 7(c)] and exhibits two peaks that do not coincide with the location of either atom (blue dots). When extended to 15 layers, the effective density exhibits peaks near the top and bottom interfaces with additional small

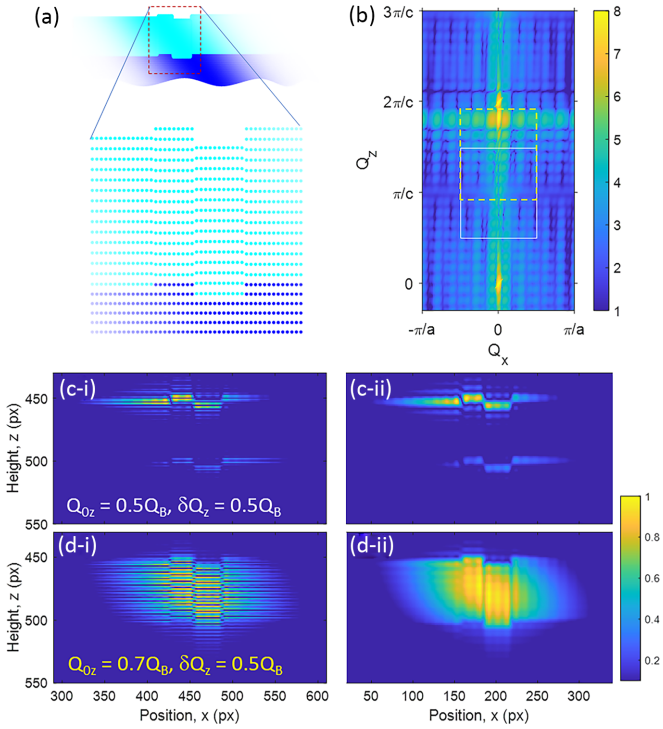

FIG. 6. Imaging supported thin films: (a) Illuminated semi-infinite interface (with the same surface topography from Fig. 2 and $\alpha = 45°$) with a 10-layer-thick epitaxial film with a vertical lattice spacing $c_{\text{film}} = 3.3$. (b) the associated reciprocal space structure (shown as $\log_{10}[I(Q_x, Q_z)]$ and calculated using Eqs. (1) and (2)). Two regions of interest (ROIs) are indicated (white box: $Q_{0z} = 0.5Q_B$, $\delta Q_z = 0.5Q_B$; yellow-dashed box: $Q_{0z} = 0.7Q_B$, $\delta Q_z = 0.5Q_B$, where $Q_B = 2\pi/c$ is the momentum transfer at the substrate Bragg peak position). The real part of the effective density is shown in rows (c) and (d), respectively, both (i) without and (ii) with the phase shift described in Fig. 4.

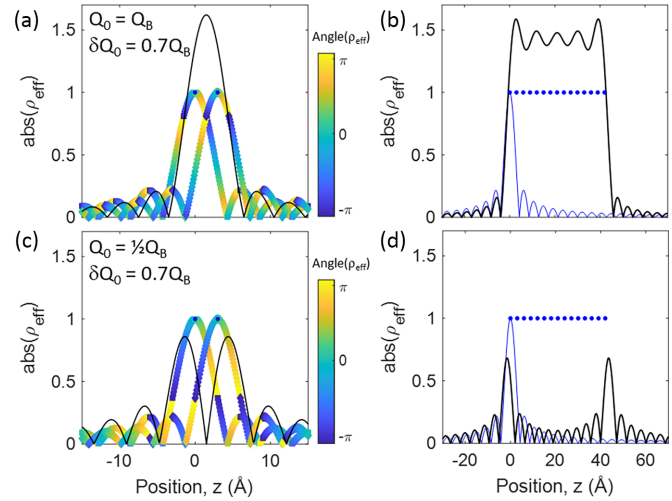

FIG. 7. Effective density as a superposition of atomic contributions: The complex effective densities for (a) two atoms (indicated as blue dots) separated by a lattice spacing c, as imaged at $Q_{0z} = Q_B$ and $\delta Q_{0z} = \frac{1}{2}Q_B$. The effective density magnitude is indicated by lines and its phase is indicated by the line color. The magnitude of the sum of the two effective densities (black line) shows that these effective densities add constructively because their phases are the same at each point within the central peak (vertical dashed lines). (b) Effective density for 1 and 15 layer films (blue and black lines, respectively) with atoms separated by c from data measured at $Q_{0z} = Q_B$ (actual atom locations are indicated by blue dots). (c) The effective density for the same two atoms separated by a lattice spacing c, as imaged at $Q_{0z} = \frac{1}{2}Q_B$ with a range $\delta Q_{0z} = \frac{1}{2}Q_B$. Note that the two atoms are out of phase by π at every point within the central peak (see dashed lines at the atom positions), and therefore, the two effective densities (black line) add destructively, and the sum cancels at the midpoint between the two atoms. (d) Effective density for 1 and 15 layer films with atoms separated by c and measured at $Q_{0z} = \frac{1}{2}Q_B$ (black line).

oscillations throughout the displayed range [Fig. 7(d)], revealing the interfacial specificity of the effective density (i.e., only the interfaces are imaged under this condition). The shape of these peaks becomes independent of the sample size once the top and bottom interfaces are separated in the effective density. Note also that the peaks at the top and bottom interfaces of the 15 layer film have a magnitude that corresponds to $\sim\frac{1}{2}$ of that for an individual atom. Furthermore, the peak position of the interfacial density is maximized at locations $\frac{1}{2}$ of a lattice spacing outside of the top and bottom layers of the film corresponding to the inflection point for the corresponding continuous density profile. This is fully consistent with the observation that the complex structure factor of a CTR at $Q_z = \pi/c$ has a value of $\frac{1}{2}$ of that corresponding to a single atomic layer and a phase factor corresponding to an outward displacement of $c/2$. Therefore, the phase for the individual atomic contributions to the density leads to effective densities that image only the interfaces of the 15-layer-thin film.

G. Spatially resolved hybrid structure factor $F(x, Q_z)$

In the previous section, we have emphasized the imaging of an interfacial topography from the phased coherent scattering data through examination of the effective density in direct space and showed how the surface topography can be extracted from those images directly. However, when the interfacial structure becomes more complex (e.g., with spatially variable interfacial structures, such as an interface with a thin-film coating whose thickness varies with position), it may not be possible, in general, to infer the relevant information from the real-space images. For instance, while the top and bottom interfaces of a thick film likely can be fully resolved, this information may become ambiguous for thin films that are not well resolved by the data. Consequently, it may be advantageous to analyze the data in reciprocal space. That is, the data can be viewed as a spatially resolved structure factor that can be obtained by inverse FT of the phased structure factors within the surface plane (or equivalently the FT of the effective densities along the direction normal to the interface):

$$F_{\text{Hybrid}}(x, Q_z) = \text{FT}^{-1}_{Q_x}\{F(Q_x, Q_z)\} = \text{FT}_z\{\rho_{\text{eff}}(x, z)\}. \quad (10)$$

Here, $\text{FT}^{-1}_{Q_x}\{\}$ indicates the inverse FT within the surface plane (i.e., along Q_x). This hybrid structure factor (along with the recovered phase information) then can be analyzed at any position on the surface x using an appropriate model. For example, the signal within an area of interest could be examined through a model-dependent analysis (like a traditional CTR

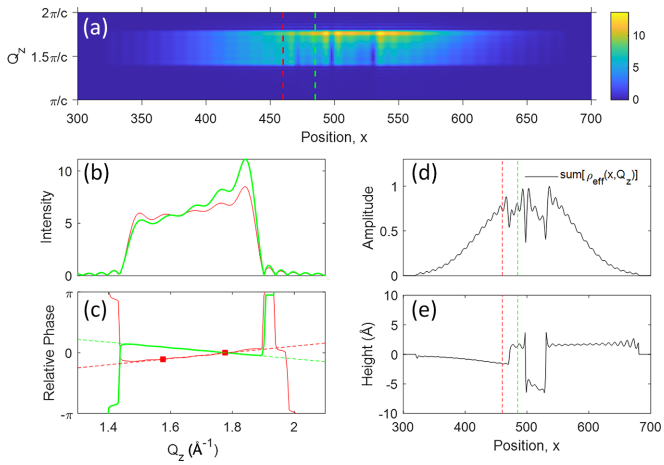

FIG. 8. The effective density as a hybrid structure factor: (a) The hybrid structure factor (as a function of position x and vertical momentum transfer Q_z) corresponding to the region of interest (ROI) at $Q_{0z} = 0.8Q_B$, $\delta Q_z = 0.2Q_B$. (b) Plot of the magnitude and (c) the phase of the hybrid structure factor at two positions [indicated in (a) by the vertical green and red dashed lines]. (d) Effective density magnitude (obtained by integrating the hybrid structure factor along Q_z). (e) Vertical phase gradient of the hybrid structure factor, corresponding to the surface height $h(x)$.

analysis but also using the recovered phases). In principle, one could analyze the structure at every nanometer-scale laterally resolved position within the approximately micron-sized illumination region. This can provide $\sim 10^5$ to 10^6 independent CTRs to reveal the nanometer-resolved interfacial structure at a level of detail comparable with that currently used to understand spatially homogenous interfaces using incoherent reflectivity.

To illustrate this concept, we use this approach to extract the surface height profile and beam illumination for the same results from Fig. 3 that were obtained above through direct analysis of the effective density ρ_{eff} (Fig. 5). The hybrid structure factor is shown in Fig. 8(a), as a function of lateral position x and vertical momentum transfer Q_z. Here, the vertical extent of the data is defined by the vertical reciprocal space window (with $Q_{0z} = Q_B$ and $\delta Q_z = 0.2Q_B$), while the lateral extent of the data (along x) is controlled by the beam illumination. Plots of the phase and intensity at two points on the surface [indicated by red and green vertical dashed lines, in Fig. 8(a)] show the increasing intensity of the CTR as a function of Q_z and the cutoff of the window function near $Q_z = 1.4$ and $1.9\,\text{Å}^{-1}$ [Fig. 8(b)] defined by the ROIs of the original data. The integrated area of this signal at each position is then plotted as a function of position [Fig. 8(d)], where we recover the same amplitude that was obtained directly from the effective densities.

The scattering phase as a function of Q_z is shown [Fig. 8(c)] at the same two locations on the surface. As can be seen, the phase gradient as a function of Q_z is clearly different for the two positions. Considering a system with a locally uniform surface but with a variation of interfacial topography, a simple structure factor model (ignoring beam illumination) suggests that the hybrid structure factor for a surface with a variable height $h(x)$ should have a functional form of $F(x, Q_z) \approx F_{\text{CTR}}(Q_z) \exp[iQ_z h(x)c]$. This implies that the structure factor phase will vary as $\phi = Q_z h(x)c$, and consequently, $h(x) = (1/c)\, d\phi/dQ_z$. The recovered height profile [Fig. 8(e)] provides the same topographic information obtained by analysis of the phase-corrected effective density (Fig. 5). While this simple example shows how the topographic information can be obtained from the hybrid structure factor, extensions of this same approach could be used to understand more complex interfacial details (e.g., film thickness, composition).

H. Experimental details/kinematics

We have so far used simulated data in which the individual pixels are arranged on an orthogonal grid, as is required for efficient transformation of the data between reciprocal and direct spaces by using FFTs. Specifically, phase retrieval algorithms require, at minimum, a twofold oversampling to provide a unique and robust retrieval of the phases [3,4,35]. The oversampling ratio is calculated as the ratio of the real-space Fourier window size $2\pi/\delta Q$ (where δQ is the data point spacing in reciprocal space) to the sample size.

In an actual experiment, the data are registered through a rocking scan, consisting in varying slightly the incidence angle by small angular steps δ_θ to record a series of 2D parallel slices of the diffracted intensity distribution with the detector around a specific point of the reciprocal space. In the resulting dataset, the arrangement of data pixels within a given detector image (defined by the directions $\mathbf{u}_{T1}$ and $\mathbf{u}_{T2}$, within and transverse to the scattering plane) is not orthogonal to either the momentum transfer $\mathbf{Q}_{0z}$ or the scan direction $\mathbf{u}_{//}$. This is a consequence of the tilt of the Ewald sphere (i.e., the detector plane in reciprocal space). For specular reflectivity, the Ewald sphere is tilted by an angle α with respect to the momentum transfer [Fig. 9(a)]. As a result, the data are collected in a nonorthogonal reference frame, and their inversion will produce a distorted image of the object. A general solution for this issue accounts for the nonorthogonal reference frame of the data defined by the vectors $\mathbf{u}_{//}$ and $\mathbf{u}_{T1}$ into an orthogonal reference frame [36,37].

Here, we provide a brief description of the oversampling constraints as a function of the beam size σ_b, film thickness Δ_f, the angular size of the detector pixels $\delta_{2\theta}$, and the rocking scan point spacing δ_θ for the case of specular reflectivity [Fig. 9(b)]. The detector angular pixel spacing $\delta_{2\theta}$ defines the reciprocal space sampling frequency within the detector plane. Thus, the pixel spacing in reciprocal space $\Delta Q_{T1} = k\delta_{2\theta}$ corresponds to a real-space window size $\Delta r_{T1} = 2\pi/\Delta Q_{T1}$ in that direction [Fig. 9(b)]. The degree of oversampling is then determined by the ratio of this window size with the sample size projected onto the detector plane (i.e., transverse to the exit beam) $\sigma_b + 2\Delta_f \cos(\alpha)$. In this expression, the first term is due to the incident beam illumination of the surface, and the second term accounts for the finite film thickness Δ_f [Fig. 9(b)]. An m-fold oversampling condition $\Delta r_{T1} = m[\sigma_b + 2\Delta_f \cos(\alpha)]$ then determines the necessary detector pixel size:

$$\delta_{2\theta} = \frac{2\pi}{mk[\sigma_b + 2\Delta_f \cos(\alpha)]}. \tag{11a}$$

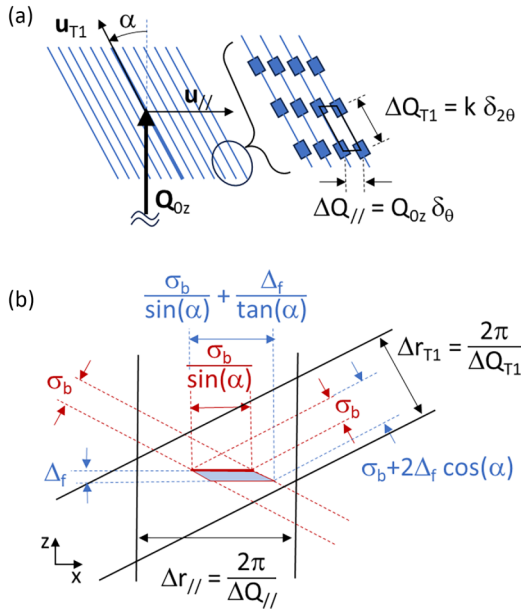

FIG. 9. Assessing conditions for oversampling: (a) Sampling of the reciprocal space near the specular reflection condition through a rocking scan. The Ewald sphere (blue lines) indicated for multiple incident angles around α is tilted with respect to the direction momentum transfer $\mathbf{Q}_{0z}$ and scanned along $\mathbf{u}_{//}$. The inset at right indicates the nonorthogonal detector pixel arrangement. (b) Schematic of the real-space Fourier window size (black lines) within the surface and detector planes ($\Delta r_{//}$ and Δr_{T1}). Also shown is the imaged object. The size of the illuminated surface (bold red line) is controlled by the incident beam width (σ_b) and the subsurface film thickness Δ_f (pale blue region). Projections of the illuminated sample size within the surface plane and transverse to the reflected beam direction are indicated for the case without and with a surface film (red and blue, respectively).

Similarly, the angular data point spacing in the rocking scan δ_θ corresponds to a reciprocal space sampling frequency $\Delta Q_{//} = Q_{0z}\delta_\theta$ along $\mathbf{u}_{//}$. The resulting lateral Fourier window size in real space is $\Delta r_{//} = 2\pi/\Delta Q_{//}$. This can be compared with a lateral sample size of $\sigma_b/\sin(\alpha) + \Delta_f/\tan(\alpha)$. Consequently, the condition for m-fold oversampling within the surface plane (i.e., along x) becomes

$$\delta_\theta = \frac{\pi}{mk[\sigma_b + \Delta_f \cos(\alpha)]}. \tag{11b}$$

Notice that, in the limit of $\Delta_f = 0$, the two equations are equivalent if $\delta_\theta = \delta_{2\theta}/2$. Furthermore, these relations reveal how a sample with a finite film thickness Δ_f alters the oversampling constraints with respect to a simple terminated surface by requiring a smaller angular sampling of the data (both $\delta_{2\theta}$ and δ_θ) to maintain the same degree of oversampling that would be achieved with an isolated surface.

There is one special case that is of interest. As seen in Fig. 9, the oversampling condition within the detector plane Δr_{T1} can be sufficient to image a projection of the sample onto the detector plane. Therefore, interfacial imaging of a surface using a single detector image would be possible as a projection of the object observed from the detector perspective [10,11] in a similar fashion as that for Bragg projection ptychographic imaging [32]. In this case, the interfacial image reveals primarily the locations of steps and the local step contrast (i.e., as shown in Fig. 5) in essentially the same way as XRIM [28,29]. In contrast, the use of full 3D datasets, as described above, maintains direct sensitivity to the interfacial topography since it observes the surface as a 3D object.

We now consider the experimental constraints on a measurement to ensure the oversampling of the intensities that are needed to invert the scattering data. Specifically, we consider the case of otavite ($CdCO_3$) films epitaxially grown on dolomite ($Ca_{1/2}Mg_{1/2}CO_3$) substrates [38,39], with vertical bulk lattice spacings of 2.96 and 2.88 Å, respectively. Measurements performed at a photon beam energy of $E = 10$ keV near a vertical momentum transfer corresponding to the otavite thin-film Bragg peak (at $Q_z = 2.13\,\text{Å}^{-1}$) would have an incident beam angle of $\alpha = 12.1°$. For the case where the detector has a pixel size of $\delta_{px} = 75\,\mu\text{m}$ positioned $R_{\text{det}} = 1700$ mm from the sample, the pixels subtend an angle of $\delta_{2\theta} = \delta_{px}/R_{\text{det}}$ (i.e., 0.0025°), corresponding to a spacing in reciprocal space of $\delta Q_{T1} = k\delta_{2\theta} = 2.2 \times 10^{-4}\,\text{Å}^{-1}$ and a window size of $\Delta r_{T1} = 2\pi/\delta Q_{T1} = 2.8\,\mu\text{m}$. A rocking scan that uses an angular point spacing δ_θ that is one-half of the corresponding to the detector pixel size ($\delta_\theta = \delta_{2\theta}/2 = 0.00125°$) corresponds to a lateral point spacing in reciprocal space of $\delta Q_{T1} = Q_{0z}\delta_\theta = 2.2 \times 10^{-4}\,\text{Å}^{-1}$ within the surface plane, corresponding to a real-space window size $\Delta r_{//} = 13.1\,\mu\text{m}$. Consequently, the twofold oversampling condition is satisfied if the beam size is smaller than half the Fourier window size or $\sigma_b < 1.4\,\mu\text{m}$ (when there is no surface film) [2,4,35]). For an interface that is coated with a 200-nm-thick film, the necessary beam size is reduced to $\sigma_b < 1.2\,\mu\text{m}$. These focusing conditions can be readily achieved with current x-ray optics, including compound refractive lenses, x-ray zone plates, and KB mirrors [40].

Another key experimental parameter is the degree of coherence of the beam and its effect on low signal-to-noise ratio scattering systems such as interfaces [41]. In the case of partially coherent beam in the transverse direction, we expect, as described for BCDI [42], a blurring of the diffraction pattern which would lead to a loss of speckle visibility. This effect reduces the spatial extent of the system which can be reconstructed, which becomes comparable with the transversal coherence length. Even for fourth-generation synchrotrons, where the transversal coherence length is >10 μm, partial coherence considerations may need to be included in the reconstruction strategies to improve the poor convergence abilities of phase retrieval algorithms when inverting partially coherent diffraction patterns [43–45]. In the case of partial longitudinal coherence arising from an incomplete monochromaticity of the beam, the effect that we expect is like the one produced by a pink beam. A pink beam consists of a beam containing a finite bandwidth ($\Delta E/E = 1.3 \times 10^{-2}$) [16,46] of the radiation spectrum. When a pink beam illuminates the sample, there is not a single momentum transfer Q but a range of them which is simultaneously probed. This could lead to a method of sampling the reciprocal space corresponding to a multiplexing of the intensity along the CTR. The scanning of the beam wavelength rather than the rocking angle to sample the reciprocal space has also been explored in the BCDI geometry [47].

IV. CONCLUSIONS

In this paper, we describe how coherent x-ray data can be used to image interfaces using 3D data volumes. In this paper, we incorporate the relevant details of the measurement using calculated scattering intensities obtained by atomistic model structures. Coherent images of the interface obtained from phased intensities of the truncation rod of a substrate or thin film reveal an effective density corresponding to the interface(s) if the associated Bragg peaks are not included. While the surface topography $h(x)$ is evident in the vertical shift of the effective densities as a function of position x, the specific shape of the effective densities are, however, strongly influenced by the Q range that is used. This includes modulations whose period is controlled by the average data window location Q_0 and within an envelope function whose width is controlled by the window range δQ. These features can be removed by multiplying the complex effective density with a phase factor, so that the interface is observed as a continuous density profile, in which the surface height corresponds to the location of the maximum of the density profile as a function of height z at each point on the surface x. These ideas are illustrated for the case of an isolated thin film, a substrate surface, and a coherently strained epitaxial thin film supported by a substrate. The mechanism for interfacial sensitivity is assessed with a simple model that considers the effective density as a sum of the contributions from each layer in the lattice. We also describe how the complex structure factors can be analyzed as a hybrid structure factor (i.e., a spatially resolved CTR), using the surface topography as an example. These results demonstrate how interfacial structure and topography can be understood once the phases of the measured intensities are recovered with phase retrieval algorithms.

ACKNOWLEDGMENTS

This paper was primarily funded by the U.S. Department of Energy, Office of Science, Office of Basic Energy Sciences, Chemical Sciences, Geosciences program (FWP#57814) under Contract No. DE-AC02-06CH11357 to UChicago Argonne, LLC as operator of Argonne National Laboratory. I.C.-A. would also like to acknowledge the European Funding "Next Generation EU" through the program "María Zambrano," a joint effort of the University of Zaragoza and the Spanish University Council (published on the 24th of July of 2021). She also acknowledges financial support from the Spanish Agencia Estatal de Investigación, through Project No. PID2020-115159GB-I00/AEI/10.13039/501100011033 and Aragonese Project No. RASMIA E12-23R cofunded by Fondo Social Europeo of the European Union FEDER (ES).

[1] D. Sayre, Some implications of a theorem due to Shannon, Acta Cryst. **5**, 843 (1952).

[2] J. R. Fienup, Reconstruction of an object from the modulus of its Fourier transform, Opt. Lett. **3**, 27 (1978).

[3] J. Miao and D. Sayre, On possible extensions of x-ray crystallography through diffraction-pattern oversampling, Acta Cryst. A **56**, 596 (2000).

[4] J. Miao, D. Sayre, and H. N. Chapman, Phase retrieval from the magnitude of the Fourier transforms of nonperiodic objects, J. Opt. Soc. Am. A **15**, 1662 (1998).

[5] J. W. Miao, P. Charalambous, J. Kirz, and D. Sayre, Extending the methodology of x-ray crystallography to allow imaging of micrometre-sized non-crystalline specimens, Nature (London) **400**, 342 (1999).

[6] M. A. Pfeifer, G. J. Williams, I. A. Vartanyants, R. Harder, and I. K. Robinson, Three-dimensional mapping of a deformation field inside a nanocrystal, Nature (London) **442**, 63 (2006).

[7] G. J. Williams, M. A. Pfeifer, I. A. Vartanyants, and I. K. Robinson, Three-dimensional imaging of microstructure in Au nanocrystals, Phys. Rev. Lett. **90**, 175501 (2003).

[8] I. K. Robinson, I. A. Vartanyants, G. J. Williams, M. A. Pfeifer, and J. A. Pitney, Reconstruction of the shapes of gold nanocrystals using coherent x-ray diffraction, Phys. Rev. Lett. **87**, 195505 (2001).

[9] I. A. Vartanyants, J. A. Pitney, J. L. Libbert, and I. K. Robinson, Reconstruction of surface morphology from coherent x-ray reflectivity, Phys. Rev. B **55**, 13193 (1997).

[10] C. H. Zhu, R. Harder, A. Diaz, V. Komanicky, A. Barbour, R. Xu, X. Huang, Y. Liu, M. S. Pierce, A. Menzel *et al.*, Ptychographic x-ray imaging of surfaces on crystal truncation rod, Appl. Phys. Lett. **106**, 101604 (2015).

[11] M. S. Pierce, V. Komanicky, A. Barbour, D. C. Hennessy, J. D. Suc, A. Sandy, C. Zhu, and H. You, *In-situ* coherent x-ray scattering and scanning tunneling microscopy studies of hexagonally reconstructed Au(001) in electrolytes, ECS Trans. **35**, 71 (2011).

[12] X. J. Huang, R. Harder, S. Leake, J. Clark, and I. Robinson, Three-dimensional Bragg coherent diffraction imaging of an extended ZnO crystal, J. Appl. Cryst. **45**, 778 (2012).

[13] M. V. Holt, S. O. Hruszkewycz, C. E. Murray, J. R. Holt, D. M. Paskiewicz, and P. H. Fuoss, Strain imaging of nanoscale semiconductor heterostructures with x-ray Bragg projection ptychography, Phys. Rev. Lett. **112**, 165502 (2014).

[14] S. O. Hruszkewycz, M. V. Holt, C. E. Murray, J. Bruley, J. Holt, A. Tripathi, O. G. Shpyrko, I. McNulty, M. J. Highland, and P. H. Fuoss, Quantitative nanoscale imaging of lattice distortions in epitaxial semiconductor heterostructures using nanofocused x-ray Bragg projection ptychography, Nano Lett. **12**, 5148 (2012).

[15] S. K. Sinha, Z. Jiang, and L. B. Lurio, X-ray photon correlation spectroscopy studies of surfaces and thin films, Adv. Mater. **26**, 7764 (2014).

[16] G. Ju, D. Xu, M. J. Highland, C. Thompson, H. Zhou, J. A. Eastman, P. H. Fuoss, P. Zapol, H. Kim, and G. B. Stephenson, Coherent x-ray spectroscopy reveals the persistence of island arrangements during layer-by-layer growth, Nat. Phys. **15**, 589 (2019).

[17] R. L. Headrick, J. G. Ulbrandt, P. Myint, J. Wan, Y. Li, A. Fluerasu, Y. Zhang, L. Wiegart, and K. F. Ludwig Jr., Coherent x-ray measurement of step-flow propagation during growth on polycrystalline thin film surfaces, Nat. Commun. **10**, 2638 (2019).

[18] I. Dax, I. A. Zaluzhnyy, A. Pylypenko, N. Russegger, V. Starostin, R. Rysov, F. Westermeier, M. Sprung, A. Hinderhofer, L. Pithan *et al.*, Insight into heterogeneous dynamics of growing islands using coherent x-ray scattering, New J. Phys. **25**, 103033 (2023).

[19] J. G. Ulbrandt, M. G. Rainville, C. Wagenbach, S. Narayanan, A. R. Sandy, H. Zhou, K. F. Ludwig, and R. L. Headrick, Direct measurement of the propagation velocity of defects using coherent x-rays, Nat. Phys. **12**, 794 (2016).

[20] M. Eriksson, J. F. van der Veen, and C. Quitmann, Diffraction-limited storage rings—A window to the science of tomorrow, J. Synchrotron Radiat. **21**, 837 (2014).

[21] R. Dimper, H. Reichert, P. Raimondi, L. S. Ortiz, F. Sette, J. Susini *et al.*, ESRF Upgrade Programme Phase II (2015–2022), Technical design study, European Radiation Synchrotron Facility, Grenoble France (2015).

[22] T. E. Fornek, Advanced photon source upgrade project final design report (IL, USA, 2019).

[23] P. Li, M. Allain, T. A. Grünewald, M. Rommel, A. Campos, D. Carbone, and V. Chamard, 4th generation synchrotron source boosts crystalline imaging at the nanoscale, Light-Sci. Appl. **11**, 73 (2022).

[24] F. Perakis and C. Gutt, Towards molecular movies with x-ray photon correlation spectroscopy, Phys. Chem. Chem. Phys. **22**, 19443 (2020).

[25] S. Streiffer, S. Vogt, and P. Evans, Early science at the upgraded Advanced Photon Source, Report to the Department of Energy, Office of Science (2015).

[26] J. Als-Nielsen and D. McMorrow, *Elements of Modern X-Ray Physics* (John Wiley and Sons, Chichester, 2001).

[27] P. Fenter, Direct recovery of interfacial topography from coherent x-ray reflectivity: Model calculations for a 1D interface, Acta Cryst. A **76**, 458 (2020).

[28] P. Fenter, C. Park, Z. Zhang, and S. Wang, Observation of subnanometre-high surface topography with x-ray reflection phase-contrast microscopy, Nat. Phys. **2**, 700 (2006).

[29] P. Fenter, C. Park, V. Kohli, and Z. Zhang, Image contrast in x-ray reflection interface microscopy: Comparison of data with model calculations and simulations, J. Synchrotron Radiat. **15**, 558 (2008).

[30] R. W. Gerchberg and W. O. Saxton, A practical algorithm for the determination of the phase from image and diffraction plane pictures, Optik **35**, 237 (1972).

[31] J. R. Fienup, Phase retrieval algorithms—A comparison, Appl. Opt. **21**, 2758 (1982).

[32] S. O. Hruszkewycz, Q. Zhang, M. V. Holt, M. J. Highland, P. G. Evans, and P. H. Fuoss, Structural sensitivity of x-ray Bragg projection ptychography to domain patterns in epitaxial thin films, Phys. Rev. A **94**, 043803 (2016).

[33] C. Jacobsen, *X-Ray Microscopy* (Cambridge University Press, Cambridge, 2020).

[34] I. A. Vartanyants and I. K. Robinson, Partial coherence effects on the imaging of small crystals using coherent x-ray diffraction, J. Phys.: Condens. Matter **13**, 10593 (2001).

[35] I. K. Robinson and J. W. Miao, Three-dimensional coherent x-ray diffraction microscopy, MRS Bull. **29**, 177 (2004).

[36] P. Li, S. Maddali, A. Pateras, I. Calvo-Almazan, S. O. Hruszkewycz, W. Cha, V. Chamard, and M. Allain, General approaches for shear-correcting coordinate transformations in Bragg coherent diffraction imaging. Part II, J. Appl. Cryst. **53**, 404 (2020).

[37] S. Maddali, P. Li, A. Pateras, D. Timbie, N. Delegan, A. L. Crook, H. Lee, I. Calvo-Almazan, D. Sheyfer, W. Cha *et al.*, General approaches for shear-correcting coordinate transformations in Bragg coherent diffraction imaging. Part I, J. Appl. Cryst. **53**, 393 (2020).

[38] E. B. R. Callagon, S. S. Lee, P. J. Eng, N. Laanait, N. C. Sturchio, K. L. Nagy, and P. Fenter, Heteroepitaxial growth of cadmium carbonate at dolomite and calcite surfaces: Mechanisms and rates, Geochim. Cosmochim. Acta **205**, 360 (2017).

[39] E. Callagon-La Plante, P. J. Eng, S. S. Lee, N. C. Sturchio, K. L. Nagy, and P. Fenter, Evolution of strain in heteroepitaxial cadmium carbonate overgrowths on dolomite, Cryst. Growth Des. **18**, 2871 (2018).

[40] X. Ou, X. Chen, X. Xu, L. Xie, X. Chen, Z. Hong, H. Bai, X. Liu, Q. Chen, L. Li *et al.*, Recent development in x-ray imaging technology: Future and challenges, Research **2021**, 9892152 (2021).

[41] G. Renaud, R. Lazzari, and F. Leroy, Probing surface and interface morphology with grazing incidence small angle x-ray scattering, Surf. Sci. Rep. **64**, 255 (2009).

[42] J. N. Clark, X. Huang, R. Harder, and I. K. Robinson, High-resolution three-dimensional partially coherent diffraction imaging, Nat. Commun. **3**, 993 (2012).

[43] G. J. Williams, H. M. Quiney, A. G. Peele, and K. A. Nugent, Coherent diffractive imaging and partial coherence, Phys. Rev. B **75**, 104102 (2007).

[44] M. S. del Rio, R. Celestre, J. Reyes-Herrera, P. Brumund, and M. Cammarata, A fast and lightweight tool for partially coherent beamline simulations in fourth-generation storage rings based on coherent mode decomposition, J. Synchrotron Radiat. **29**, 1354 (2022).

[45] B. Chen, B. Abbey, R. Dilanian, E. Balaur, G. van Riessen, M. Junker, C. Q. Tran, M. W. M. Jones, A. G. Peele, I. McNulty *et al.*, Diffraction imaging: The limits of partial coherence, Phys. Rev. B **86**, 235401 (2012).

[46] G. X. Ju, M. J. Highland, C. Thompson, J. A. Eastman, P. H. Fuoss, H. Zhou, R. Dejus, and G. B. Stephenson, Characterization of the x-ray coherence properties of an undulator beamline at the Advanced Photon Source, J. Synchrotron Radiat. **25**, 1036 (2018).

[47] W. Cha, A. Ulvestad, M. Allain, V. Chamard, R. Harder, S. J. Leake, J. Maser, P. H. Fuoss, and S. O. Hruszkewycz, Three dimensional variable-wavelength x-ray Bragg coherent diffraction imaging, Phys. Rev. Lett. **117**, 225501 (2016).